Deconvolution of Axial Velocity Distributions from Hall Thruster LIF Spectra [*†]

Timothy B. Smith, Daniel A. Herman[‡],
Alec D. Gallimore[§] and R. Paul Drake[¶]
Plasmadynamics and Electric Propulsion Laboratory
University of Michigan
Rm. B107, 1919 Green Rd.
Ann Arbor, MI 48105
734-764-4199
timsmith@umich.edu

IEPC-01-0019

Abstract

We present laser-induced fluorescence (LIF) measurements of Xe II ($^4D_{7/2}$) downstream of the P5 Hall thruster at 1.6 kW and 3.0 kW operating conditions. A novel deconvolution method allows direct extraction of beamwise velocity distributions $f(v_k)$ from LIF spectra at 605.1 nm. Maxwellian curve-fits to distributions from axial-injection LIF give temperatures and bulk velocity components in orthogonal axes without the angular error propagation characteristic of multiplex LIF. Axial profiles of axial ion velocity show a zone of increasing velocity extending 20 cm downstream of the thruster exit plane, with decreasing velocity from 20 to 50 cm. Transformation of deconvolved velocity distributions to energy space shows a marked similarity between results from LIF and molecular beam spectroscopy at similar locations. Two-dimensional velocity distributions reconstructed from vertical and axial distributions show strong interactions between counter-flowing streams in the inward divergence region at the thruster centerline.

1 Introduction

Laser-induced fluorescence (LIF) has seen a recent upswing in popularity as a non-intrusive plume diagnostic, from early characterization of hydrogen arcjets[1, 2] to more recent studies of xenon Hall thruster plumes[3, 4, 5, 6]. Traditional intrusive probes such as Langmuir probes, retarding potential analyzers (RPAs), and molecular beam mass spectrometers (MBMSs) perturb the plasma, yielding data that may not be representative of the actual thruster performance.

The current state-of-the-art in LIF, the multiplex technique pioneered by Keefer *et al.*[1] and further developed by Williams[6], focuses two to four beams through a single lens. The data analysis routine fits LIF spectra from each beam to a simulated signal, calculated by convolving the hyperfine and isotopic line structure of the absorption transition with a drifting Maxwellian velocity distribution. By varying the bulk velocity and temperature of this distribution, the routine obtains a best fit to the data. Basic trigonometry and some simple kinetics assumptions then allow the transformation of bulk velocities and temperatures in the beam axes to an orthogonal coordinate system tied to the thruster axes.

This method has three major flaws. First, it implic-

[*] Presented as Paper IEPC-01-0019 at the 27th International Electric Propulsion Conference, Pasadena, CA, 15-19 October 2001.

[§] Graduate students, PEPL

[¶] Associate Professor and Director, PEPL

[‖] Professor and Director, Space Physics Research Laboratory

itly assumes that the interrogated species population is at equilibrium. This equilibrium assumption grows increasingly unwarranted as we approach the ion creation zone. Furthermore, recent measurements at the centerline of a Hall thruster[6] suggest the presence of counterstreaming plasmas, with at least two distinct populations. Clearly, a single Gaussian is a poor fit to these, more complex, velocity distributions.

Second, the small laser beam convergence angles required by the multiplex method can cause significant errors in transforming bulk velocities to an orthogonal coordinate system. Consider the beam propagation and orthogonal axes shown in Fig. 1, where the "axial" beam enters downstream of the lens center at an angle α from the vertical beam. In this case, the true axial velocity

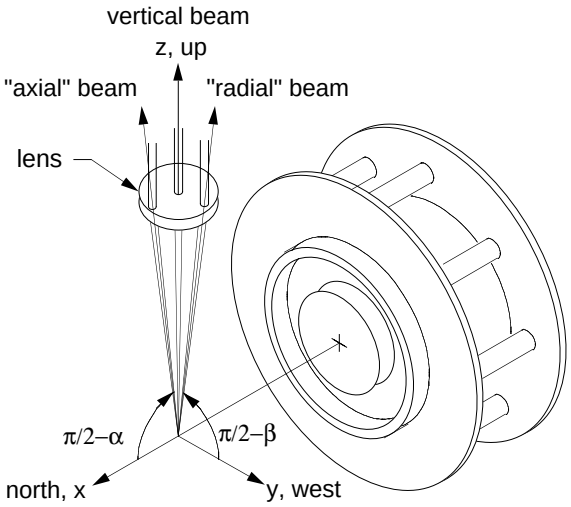

Figure 1: Beam and thruster orthogonal axes.

component u_x can be transformed from the vertical velocity u_z and the "axial" velocity u_a by

$$u_x = \frac{u_a - u_z \cos\alpha}{\sin\alpha}. \tag{1}$$

Not only does this mean that random error in beamwise velocities is multiplied by $1/\sin\alpha$, but the proportional error with respect to angular error is

$$\frac{1}{u_x}\frac{\partial u_x}{\partial \alpha} = \frac{u_z}{u_x} - \cot\alpha. \tag{2}$$

Thus, both velocity errors and angular errors diverge rapidly at small angles. For instance, at $\alpha = 10^\circ$, independant 2% random errors in u_z and u_a, combined with a 2% bias in angular measurement, result in a 20% error in the calculated axial velocity u_x.

Finally, in order to transform the temperature from beam axes to an orthogonal coordinate system, we must assume statistical independance of the axial and vertical velocity distributions; *i.e*, $f(x,z) = f_x(x)f_z(z)$. Any tilting of the two-dimensional velocity distribution contours with respect to the thruster axes makes this assumption invalid.

We have developed an approach that addresses all three of these problems with the multiplex method. Since the LIF signal is a convolution of a known line structure and an unknown velocity distribution, it follows that the velocity distribution along a given line of sight can be deconvolved from a LIF signal along that line of sight. We have developed a simple, Fourier-transform deconvolution method for this purpose, which sidesteps the assumption of equilibrium. Instead of using the multiplex setup illustrated in Fig. 1, we have conducted experiments in which we injected the laser beam directly along the thruster orthogonal axes. We will refer to such measurements along the thruster axis as "axial-injection LIF" and in the horizontal plane as "lateral-injection LIF". Deconvolution of direct axial-injection and lateral-injection LIF spectra returns axial and lateral velocity distributions. When appropriate, Maxwellian curve-fits to these distributions directly provide lateral and axial bulk velocities and temperatures.

We performed two sets of axial-injection LIF measurements from 1 mm to 50 cm downstream of the exit plane of the P5 Hall thruster over three separate days. All experiments were performed in the large vacuum test facility (LVTF) at the University of Michigan's Plasmadynamics and Electric Propulsion Laboratory (PEPL).

2 Theory

2.1 Laser Induced Fluorescence

LIF is the incoherent emission of photons from an excited state (electronic in the case of xenon or other monatomics) populated by the absorption of photons from the laser. Usually, absorption of photons at one

wavelength results in emission at several allowed wavelengths.

A single particle of the absorbing species will "see" the frequency of an incoming photon shifted by the relative motion of the particle in the direction of the photon. If the particle is moving toward the photon source, it "sees" a bluer (*i.e.*, higher-frequency) photon than a stationary particle would. This Doppler effect appears as a shift in the resonant frequency ν_o as the laser is scanned over a very short frequency range. The change in photon frequency $\triangle\nu$ for a particle with velocity $\vec{v}$ passing through a light beam of wave vector $\vec{k}$ is

$$\triangle\nu_D = -\vec{k}\cdot\vec{v}/2\pi. \tag{3}$$

Singly ionized xenon, Xe II, is the dominant species in Hall thruster plumes. Xe II has natural absorption/emission transitions throughout the visible spectrum. This series of tests used 605.1 nm light to drive the $5d^4D_{7/2} - 6p^4P^0_{5/2}$ absorption and collected emission from the $6s^4P_{5/2} - 6p^4P^0_{5/2}$ transition at 529.2 nm.

2.2 Fluorescence Lineshape Model

There are nine stable isotopes of xenon, seven of which have natural abundances greater than one percent. Each of these isotopes has a slightly different term energy at a given energy level. This energy difference results in isotopic splitting.

The two isotopes with an odd atomic mass, ^{129}Xe and ^{131}Xe, have a non-zero nuclear spin quantum number I, resulting in hyperfine splitting of the atomic energy levels. This hyperfine structure (hfs) is considerably broader than the isotopic structure, and provides most of the $5d^4D - 6p^4P^0$ transition's characteristic shape. The lighter isotope, ^{129}Xe, has $I = 1/2$, while ^{131}Xe has $I = 7/2$. The total angular momentum quantum number F takes values

$$F = I + J, I + J - 1, \ldots, |I - J| \tag{4}$$

where J is the total electronic angular momentum [7]. Figure 2 shows the fine structure and hyperfine splitting for the $^4P_{5/2} - ^4D_{7/2}$ line.

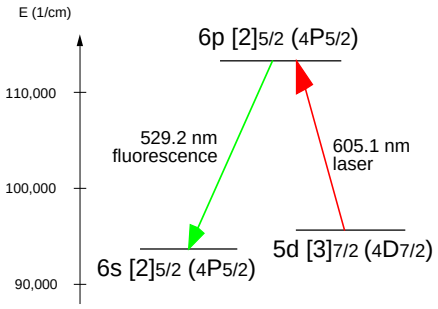

(a) Xe II LIF fine structure.

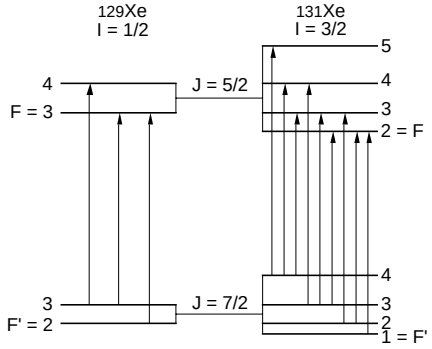

(b) Hyperfine structure of 605.1 nm absorption line.

Figure 2: Fine and hyperfine structure of Xe II LIF.

The extra term energy due to hfs is given by

$$E_{hfs} = A\frac{C}{2} + BD, \tag{5}$$

where A is the nuclear magnetic dipole interaction constant, B is the nuclear electric quadrupole interaction constant, and the terms

$$C = F(F+1) - I(I+1) - J(J+1) \tag{6}$$

and

$$D = \frac{(3C/4)(C+1) - I(I+1)J(J+1)}{2I(2I-1)J(2J-1)} \tag{7}$$

contain the nuclear spin-orbit interactions. The transition rule for hyperfine splitting is $\triangle F \equiv F - F' = [0, \pm 1]$, where F is the upper and F' is the lower state's total angular momentum quantum number. (The zero-zero transition is forbidden, $F = 0 \not\rightarrow F' = 0$.) The relative intensity of each hyperfine component is given for a $J \rightarrow J - 1$ transition by [8]

$$I(F \rightarrow F-1) \quad \propto \quad \frac{P(F)P(F-1)}{F} \tag{8}$$

$$I(F \to F) \propto \frac{(2F+1)}{F(F+1)} P(F)Q(F) \quad (9)$$

$$I(F-1 \to F) \propto \frac{Q(F)Q(F-1)}{F} \quad (10)$$

where $P(F) = (F+J)(F+J+1) - I(I+1)$ and $Q(F) = I(I+1) - (F-J)(F-J+1)$.

This model uses published isotopic shifts and hyperfine structure constants for the Xe II $^4P_{5/2}$ and $^4D_{7/2}$ energy levels[9].

For the isotopes with even mass numbers (i.e., without hfs), the line intensity p_j is linearly proportional to the naturally-occurring abundance for each isotope. The line intensities of ^{129}Xe and ^{131}Xe are linearly proportional to the product of the isotopic abundance and the relative intensity of the hyperfine components.

2.3 LIF spectrum convolution

Blurring or broadening of an object function $o(x)$ by a spread function $s(x)$ can be expressed as a convolution integral $i(x)$ of the form [10]

$$i(x) = \int_{-\infty}^{\infty} s(x-x')o(x')\,dx'. \quad (11)$$

If we denote convolution by the symbol $\otimes$, Eqn. 11 becomes

$$i(x) = s(x) \otimes o(x) \quad (12)$$

with the useful properties of commutivity and distributivity with respect to addition,

$$i_N(x) = \left[\sum_{j=1}^{N} s_j(x)\right] \otimes o(x) = \sum_{j=1}^{N} \left[s_j(x) \otimes o(x)\right]. \quad (13)$$

The conventional method of modeling line broadening around a line center ν_o convolves a Cauchy distribution $l(\nu)$ with a Gaussian $g(\nu)$ into a Voigt profile[11]

$$i(\nu) = l(\nu) \otimes g(\nu), \quad (14)$$

where the "natural" broadening

$$l(\nu) = \frac{A_{ij}}{4\pi^2[(\nu-\nu_o)^2 + (A_{ij}/4\pi)^2]} \quad (15)$$

is controlled by the transition's lifetime A_{ij}, while the Doppler broadening

$$g(\nu) = \frac{1}{\nu_o}\left(\frac{mc^2}{2\pi kT}\right)^{1/2} \exp\left(-\frac{mc^2}{2kT}\left[\frac{\nu-\nu_o}{\nu_o}\right]^2\right) \quad (16)$$

is caused by a Maxwellian velocity distribution with a temperature T. The Xe II absorption spectrum of an equilibrium plasma resolved by LIF at 605.1 nm is the the sum of $N = 17$ such lines,

$$i_N(\nu) = \mathcal{C}\sum_{j=1}^{17} p_j i_j(\nu) \quad (17)$$

where p_j is the intensity for each line j, $i_j(\nu)$ is the Voigt profile given by Eqn. 14, and $\mathcal{C}$ is a constant representing a whole series of unknowns, including plasma density, collection solid angle, monochromator throughput, photomultiplier tube efficiency, output current-to-voltage amplification and analog-to-digital converter range. The center for each line is given by

$$\nu_j = \nu_o + \triangle\nu_{\rm hfs} + \triangle\nu{\rm is} + \triangle\nu_D, \quad (18)$$

where $\nu_o = (E' - E'')/h$ is the frequency associated with the upper and lower electronic state energies E' and E'', $\nu_{\rm hfs} = (E'_{\rm hfs} - E''_{\rm hfs})/h$ is the frequency shift caused by the hyperfine term energies $E'_{\rm hfs}$ and $E''_{\rm hfs}$ given by Eqn. 5, $\triangle\nu_{\rm is}$ is the isotopic shift for the transition[9], and $\triangle\nu_D$ is the Doppler shift given by Eqn. 3.

Nonequilibrium plasmas, of course, do not necessarily have Maxwellian velocity distributions. A more general model of the LIF spectrum for an arbitrary velocity distribution $f(v)$ is given by

$$i(\nu) = \mathcal{C}\sum_{j=1}^{N} p_j l_j(\nu) \otimes f(v/\lambda_o) \quad (19)$$

where p_j is the intensity, l_j is a naturally-broadened lineshape around each of N hyperfine and isotopic lines, and λ_o is the transition wavelength. A perfectly cold (*i.e.*, naturally-broadened), stationary distribution, where $f(v) = \delta(v)$, then gives the LIF spectrum

$$c(\nu) = \mathcal{C}\sum_{j=1}^{N} p_j l(\nu) \quad (20)$$

so that the Voigt profile becomes

$$i_N(\nu) = c(\nu) \otimes f(v/\lambda_o). \quad (21)$$

2.4 Deconvolution

Given the Fourier transforms $S(\omega)$ and $O(\omega)$ of the object and spread functions $o(x)$ and $s(x)$, the convolution theorem states that the convolution

$$i(x) = s(x) \otimes o(x) \tag{22}$$

is equivalent to the product

$$I(\omega) = S(\omega)O(\omega) \tag{23}$$

where $I(\omega)$ is the Fourier transform of $i(x)$. If we define the Fourier transform pairs

$$C(\tau) \overset{\text{F.T.}}{\Longleftrightarrow} c(\nu) \tag{24}$$

$$F(\tau) \overset{\text{F.T.}}{\Longleftrightarrow} f(v/\lambda_o) \tag{25}$$

$$I(\tau) \overset{\text{F.T.}}{\Longleftrightarrow} i_N(\nu) \tag{26}$$

for the atomic line structure and velocity distribution functions, then the convolution theorem implies that

$$F(\tau) = I(\tau)/C(\tau). \tag{27}$$

The one-dimensional velocity distribution along the beam propagation direction is proportional to the inverse Fourier transform, $\mathcal{F}^{-1}$, of $F(\tau)$, converted from frequency space to velocity space:

$$f(v/\lambda_o) = \mathcal{F}^{-1}\left\{I(\tau)/C(\tau)\right\}. \tag{28}$$

2.5 Filtering and forced positivity

Deconvolution methods tend to preferentially amplify high-frequency noise[10], as shown in Fig. 3(a). Low-pass filtering of the deconvolved velocity distribution with a Gaussian function returns a smoother signal without artificially-induced ringing; the passband limit can be readily adjusted to avoid excess smoothing.

The resulting function, while much less noisy, still has negative components. Since velocity distributions are positive by definition, a positivity forcing function

$$p[f(v)] = \frac{f(v) + \sqrt{f(v)^2 + \epsilon}}{2} \tag{29}$$

is needed, where ϵ is a user-defined small positive number. Figure 3(b) shows how this function smoothly maps the filtered deconvolution to an acceptable approximation of the velocity distribution.

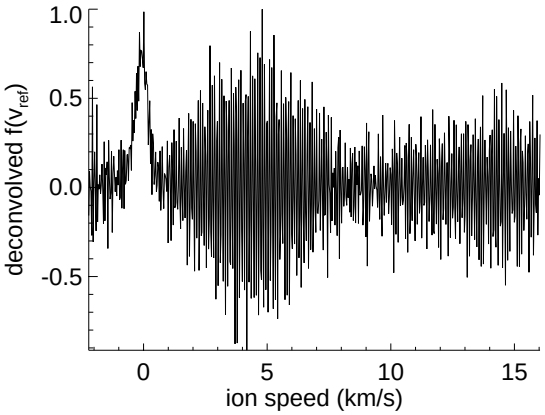

(a) Unfiltered deconvolution.

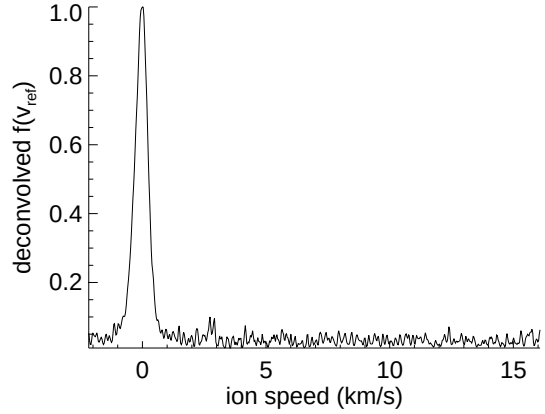

(b) Deconvolution, filtered & forced positive.

Figure 3: Typical velocity distribution $f(v)$ from stationary plasma in a xenon opto-galvanic cell .

2.6 Maxwellian curve-fitting

Most of the velocity distribution plots resulting from the deconvolution of our data can be approximated as a single drifting Maxwellian distribution,

$$f_M(v) = \left(\frac{m}{2\pi kT}\right)^{1/2} \exp\left(-\frac{m[v-u]^2}{2kT}\right) \tag{30}$$

To accomplish this, we fit data from a user-defined section of the velocity distribution (via a simple linear curve-fit to the log of the data) to a Maxwellian distribution, giving a bulk velocity u and temperature T along the beam axis.

Counterflowing plasmas, such as the lateral flow near a Hall thruster's centerline, can be approximated as the sum of two Maxwellian distributions. In this case, data defining each peak were selected for the curve-fitting routine, returning two values of u and T for the upwards (positive u_z) and downwards (negative u_z) populations.

2.7 Kinematic compression

Collisionless acceleration of an ion beam tends to cool the velocity distribution along the acceleration axis in a process known as kinematic compression[12]. Consider an ion population with an initial bulk velocity u_0 and velocity FWHM of $\triangle u_0$. A steady potential drop U will accelerate ions at the FWHM points of a distribution to

$$u_p = \sqrt{\left(u_0 + \frac{\triangle u_0}{2}\right)^2 + \frac{2eU}{m}} \quad (31)$$

$$u_m = \sqrt{\left(u_0 - \frac{\triangle u_0}{2}\right)^2 + \frac{2eU}{m}} \quad (32)$$

so that the FWHM of the accelerated beam is

$$\triangle u_1 = u_p - u_m. \quad (33)$$

Since $\triangle u_0 = 2\sqrt{2 \ln 2 \, kT_0/m}$ and $\triangle u_1 = 2\sqrt{2 \ln 2 \, kT_1/m}$, the ratio of the final axial temperature to the initial axial temperature becomes

$$\frac{T_1}{T_0} = \left(\frac{\triangle u_1}{\triangle u_0}\right)^2 \quad (34)$$

if the acceleration is collisionless and steady-state. If the ion temperature data follow the trend of Eqn. 34, we can conclude that these assumptions are supported.

3 Apparatus and Procedure

3.1 Thruster

Figure 4 shows the P5, a 5 kW class Hall thruster developed for research at the University of Michigan in conjunction with the Air Force Rocket Laboratory. Performance and probe testing[13] demonstrated performance levels and operating conditions consistent with thrusters under commercial development.

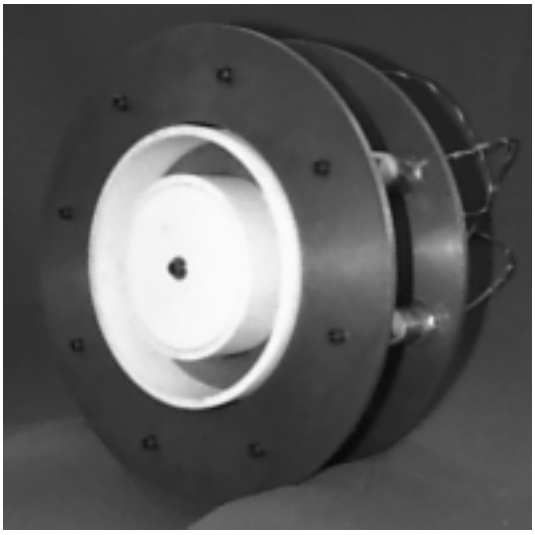

Figure 4: Photograph of the P5 Hall effect thruster.

Thruster power was provided by laboratory power supplies. The main discharge was supplied by a Sorensen DCR 600-16T. The electromagnets were powered separately, the inner by a Kikusui PAD 55-10L and the outer by a Sorensen DCS 33-33. The cathode heater was a Kepco ATE36-30M, and the igniter was a custom-built high-voltage ignition supply. The thruster discharge circuit was electrically isolated during operation. A filter consisting of 1.3 Ω equivalent resistance in series with the discharge current and a 95 μF capacitor in parallel was used to damp out thruster oscillations.

The annular discharge channel is 2.54 cm wide and is on a 7.37 cm radius. We moved the cathode, normally mounted directly above the thruster centerline, to a position roughly 45 degrees from vertical to avoid interference with the LIF optics. Table 1 gives the thruster operating conditions used in this study. Discharge voltage was held constant within the power supply measurement precision during each test. The anode and cathode flow rate settings also remained constant. The run-to-run variation of discharge current was less than 10%, while the day-to-day variation of cathode floating potential was less than 2%.

Table 1: P5 operating conditions.

	1.6 kW	3.0 kW	units
Discharge voltage	300.1	300.1	V
Anode potential	277.0	271.9	V
Cathode potential	-23.1	-28.2	V
Discharge current	5.30	10.40	A
Anode flow rate	61.0	114.0	sccm
Cathode flow rate	6.00	6.00	sccm
Facility pressure	5.5	9.7	μTorr

3.2 Facility

Tests were performed in the $\phi 6 \times 9$ m LVTF. Four of the seven available CVI Model TM-1200 Re-Entrant Cryopumps, each surrounded by a liquid nitrogen baffle, provided a xenon pumping speed measured at 140,000 l/s with a base pressure of less than 2×10^{-7} Torr. Propellant flow was controlled by two MKS Model 1100 Flow Controllers.

The P5 was positioned on a probe table, which allowed two degrees of freedom over about a meter in each direction. Though a rotational stage mounted on the probe table allowed the thruster to be slewed through 180°, laser problems terminated tests before lateral-injection tests could be performed. All three translation stages were computer-controlled, with locational resolution on the order of 0.025 cm and angular resolution on the order of 0.1 degree.

3.3 Laser and Optics

An argon-ion pumped Coherent dye laser (899-29 model) using Rhodamine-6G dye provided 350–450 mW at 605 nm. The laser wavelength was scanned over a 0.012 to 0.060 nm range (10 to 50 GHz) in 0.061 pm (50 MHz) increments. The scanning and the synchronized data collection were computer-controlled.

The laser and optics shown schematically in Fig. 5 were located in a controlled atmosphere/low-dust enclosure. Because of the large natural fluorescence at 529 nm, we chopped the laser beam at 1580 Hz to phase-lock the LIF signal. A beam splitter downstream of the chopper sent about 8 percent of the beam through the center of a Hamamatsu hollow-cathode opto-galvanic cell filled with a Xe-Ne gas mixture. A 250 V discharge across this opto-galvanic cell gave a strong Xe II signal, collected by a Chromex 500is monochromator with a Hamamatsu 928 photo-multiplier tube (PMT). Deconvolution of this signal, as shown in Fig. 3(b), provided a stationary reference for the distributions extracted from plume LIF.

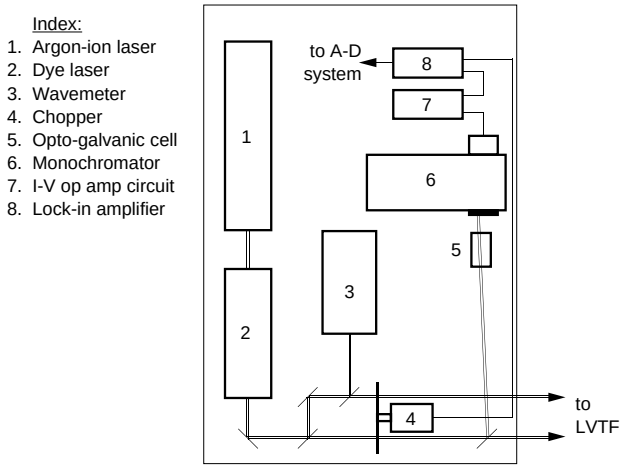

Figure 5: Laser division and modulation.

Figure 6(a) shows the LVTF beam handling setup. A three-prism periscope system, shown in Fig. 6(b), sent the beam through a focusing telescope parallel to the thruster axis, reducing the beam diameter (which had grown to approximately 2.0 cm over the 12 m path length) to less than 1 mm. An enclosure with anti-reflection (AR) coated windows protected the beam-turning prisms and focusing telescope from sputtering deposition and erosion. A focus tube between the telescope elements provided axial adjustment of the laser focus. A $\phi 1$ mm diameter steel T-pin, centered on the downstream face of the thruster, facilitated laser alignment. After placing the laser focal volume on the pin head, we adjusted the collection lens, sending a collimated beam of scattered light through the LVTF window.

Two separate AR windows protected the $\phi 100$ mm, $f/2.5$ collection lens. The collimated fluorescence from the thruster plume was focused by a $\phi 100$ mm, $f/5$ lens onto a Spex H-10 monochromator with a Hamamatsu

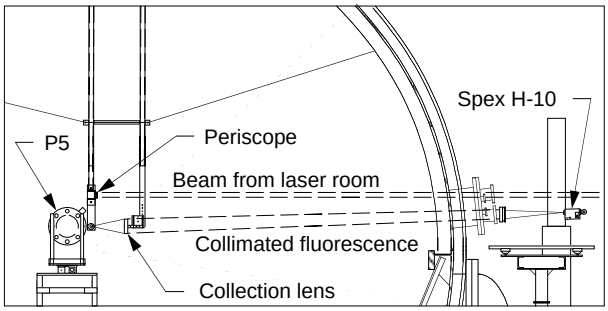

(a) Looking upstream (north) from behind thruster.

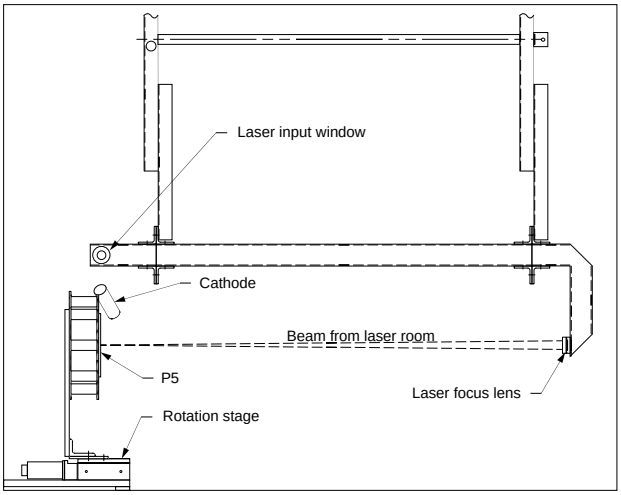

(b) Looking west.

Figure 6: Laser beam delivery and fluorescence collection optics schematic.

928 PMT. Stanford SR810 and SR850 DSP lock-in amplifiers, using a 1-second time constant, isolated the fluorescence components of these signals.

Between experiments, we brought up the LVTF to atmospheric pressure and inspected all in-chamber optics. AR windows were cleaned or replaced, as necessary. We then confirmed thruster continuity, realigned the optics and evacuated the LVTF.

The laser focal point inevitably shifted during chamber evacuation. By orienting the T-pin so that the its head's long axis was vertical, we were able to recover alignment of the laser and collection train focal points by lateral translation of the thruster and vertical translation of the H10 monochromator.

The Coherent 899-29 laser's Autoscan software collected and matched laser wavelength to the corresponding lock-in output. A scan rate of 60 s/10 GHz proved sufficiently slow to ensure a reasonable signal-to-noise ratio in most cases. For noisier signals, we collected several scans at the same scan rate, passed them through a Chauvenet's criterion[14] rejection filter, and averaged them into a single, smoother scan.

4 Results

We took three sets of data at 1.6 kW and 3.0 kW operating conditions. The first was an axial sweep from 50 cm to 0.05 cm downstream of the thruster exit plane along the P5 discharge channel axis (7.37 cm outboard of the thruster axis). The second was a 2 cm lateral sweep across the discharge channel, 1 mm downstream of the thruster exit plane. The third was an axial sweep from 5 cm to 50 cm downstream of the thruster exit plane along the thruster centerline.

Several checks for saturation and power broadening, made by inserting a neutral density filter upstream of the beam splitter, showed no systematic decrease in effective ion temperature.

4.1 Axial sweep along discharge centerline

Figure 7 shows a typical axial velocity distribution taken downstream of the discharge channel. The solid line is the deconvolved distribution, while the dashed line is a Maxwellian curve-fit to a user-defined area within the major peak. This distribution is typical of most taken downstream of the discharge channel. Repeat runs and extended laser frequency sweeps failed to pick up significant secondary populations in all but one case, shown in Fig. 8. Chauvenet-filtered averaging of four successive LIF spectra at this point ensured that this peak was not random noise.

Figures 9(a) and 9(b) show the axial variation of ion axial velocity along the P5 discharge channel axis, 7.37 cm outboard of the thruster axis. The axial velocity precision error[14] was less than 0.5% at 1.6 kW, and less than 1.0% at 3.0 kW. At 20 cm downstream of the exit plane, axial velocity hit a maximum of 18.7 km/s at 1.6

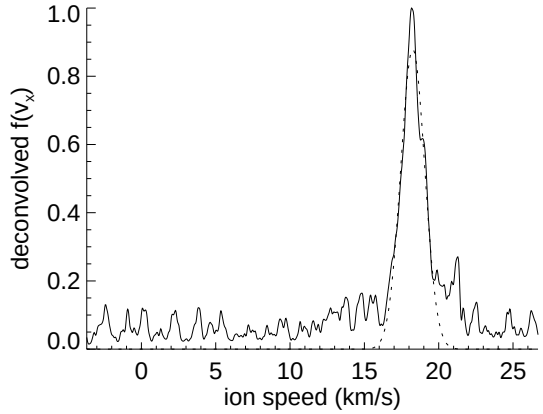

Figure 7: Deconvolved $f(v)$ (solid) & Maxwellian curve-fit (dashed) at 1.6 kW, (x, y) = (50., 7.37) cm.

kW. Figure 8 shows how a significant secondary population with a velocity of 15.0 km/s occurred at this point. The axial velocity at 3.0 kW also reached its maximum (18.7 km/s) at $x = 20$ cm, but no secondary population appears in the velocity distribution there.

Figures 10(a) and 10(b) show the same data in terms of axial energy. At 1.6 kW, axial energy rose from 133 V at $x = 5$ mm to 239 V at $x = 20$ cm, while it rose from 124 V to 237 V over the same range at 3.0 kW. Measurements at $x = 35$ cm and $x = 50$ cm showed a slight deceleration, so that by $x = 50$ cm, the axial energy had dropped to 227 V at 1.6 kW and 225 V at

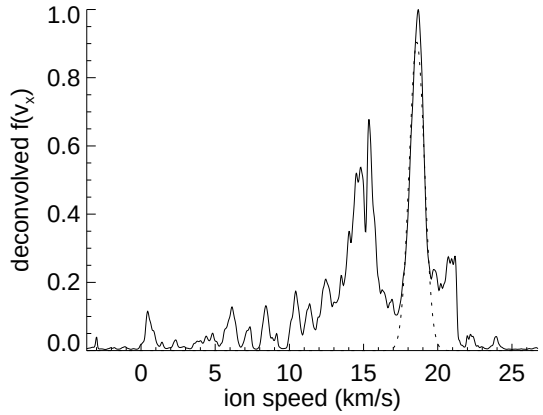

Figure 8: Twin-peaked distribution at 1.6 kW, (x, y) = (20., 7.37) cm.

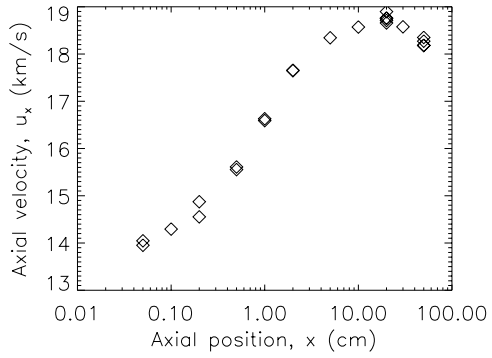

(a) 1.6 kW operating condition.

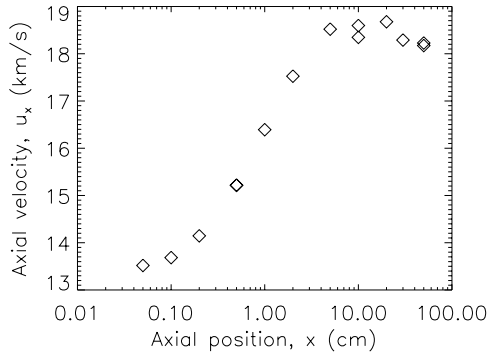

(b) 3.0 kW operating condition.

Figure 9: Axial ion velocity vs. axial position along P5 discharge centerline (y = 7.37 cm).

3.0 kW.

Figures 11(a) and 11(b) show the variation of ion axial temperature along the P5 discharge channel axis. The temperature trend at 1.6 kW roughly mirrors the velocity trend; *i.e.*, the minimum temperature (0.42 eV) is at the point of maximum velocity, while the temperature maxima are at the beginning (0.80 eV) and end (0.88 eV) of the sweep. This roughly follows the kinematic compression trend predicted by Eqn. 34. The temperature trend at 3.0 kW was more difficult to follow, but appears more-or-less linear with $\ln(x)$, rising from 0.74 eV near the exit plane to 1.68 eV at the end of the sweep. The predicted kinematic compression, if at all applicable, fails to appear past $x = 1.0$ cm. The precision error in axial temperature was considerably higher than the velocity precision error, with most points lying within a 20% uncertainty band at 1.6 kW and a 40% uncertainty

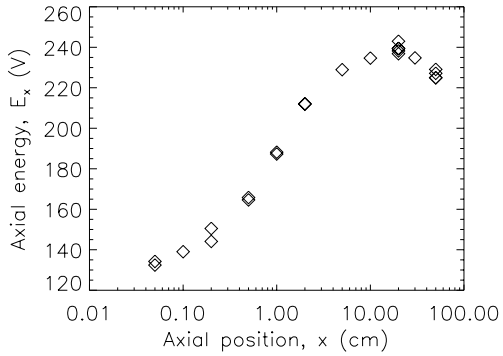

(a) 1.6 kW operating condition.

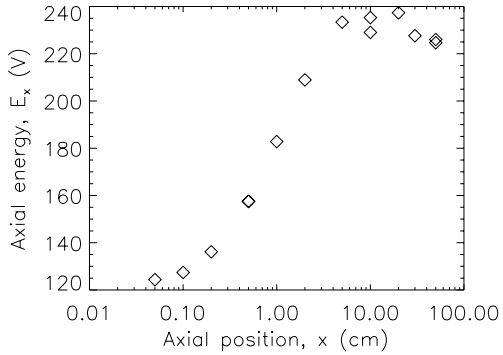

(b) 3.0 kW operating condition.

Figure 10: Axial ion energy vs. axial position along P5 discharge centerline (y = 7.37 cm).

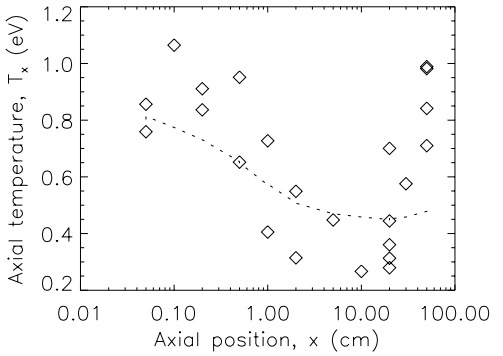

(a) 1.6 kW operating condition.

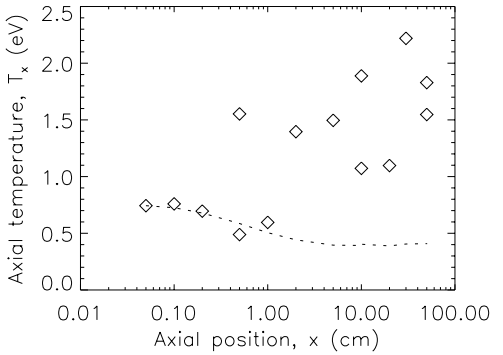

(b) 3.0 kW operating condition.

Figure 11: Axial ion temperature vs. axial position along P5 discharge centerline (y = 7.37 cm). Dashed line shows predicted kinematic compression.

band at 3.0 kW.

4.2 Lateral sweep across discharge

Figures 12(a) and 12(b) show the lateral variation of ion axial velocity along a plane 1 mm downstream of the P5 discharge channel axis. At both operating conditions, the minimum velocity is along the discharge channel centerline, with higher axial velocities at both edges of the discharge. The lateral profile at 1.6 kW ranged from 14.2 km/s to 14.7 km/s, with a precision error within 1.5%. The lateral profile at 3.0 kW is an unusually smooth, nearly parabolic curve from 13.7 km/s to 14.1 km/s, with precision error well below 0.02%.

Figures 13(a) and 13(b) show the variation of ion axial temperature along a plane 1 mm downstream of the P5 discharge channel axis. No clear trend is visible in the 1.6 kW data, while the 3.0 kW trend is largely flat around 0.72 eV.

4.3 Axial sweep along thruster centerline

Figures 14(a) and 14(b) show reconstructions of the two-dimensional velocity distribution $f(v_x, v_z)$ directly downstream of the P5 centerline at 10 cm and 50 cm. These reconstructions are based on an assumption of statistical independance of the axial and vertical distributions,

$$f(v_x, v_z) = f_x(v_x) f_z(v_z) \tag{35}$$

where the vertical distributions are taken from recent (unpublished) multiplex LIF measurements of the P5

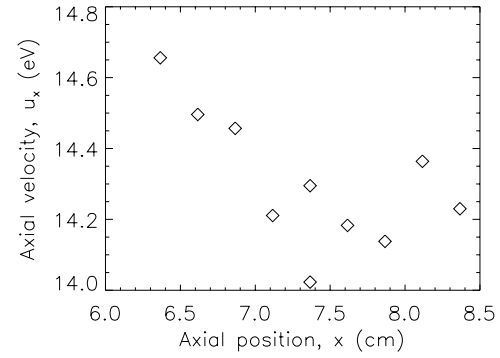

(a) 1.6 kW operating condition.

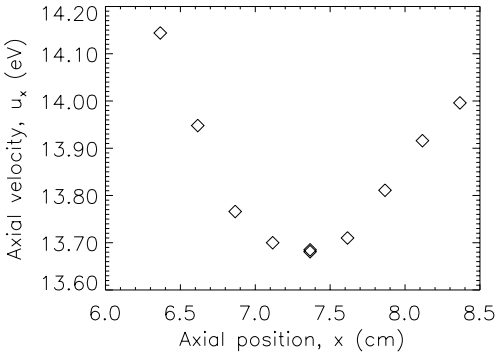

(b) 3.0 kW operating condition.

Figure 12: Axial ion velocity vs. lateral position 1 mm downstream of P5 discharge (x = 0.1 cm).

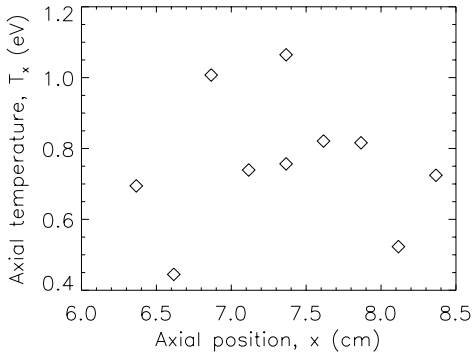

(a) 1.6 kW operating condition.

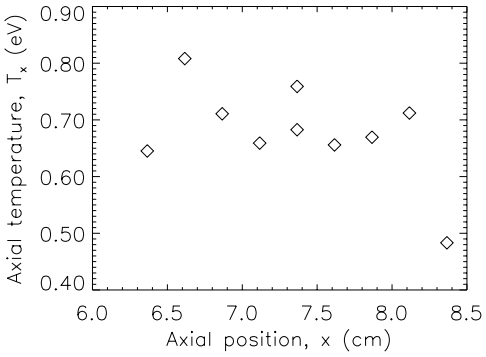

(b) 3.0 kW operating condition.

Figure 13: Axial ion temperature vs. lateral position 1 mm downstream of P5 discharge (x = 0.1 cm).

plume at 3.0 kW.

The $x = 10$ cm reconstruction in Figure 14(a) shows counterflowing plasmas with a mean axial velocity of 15.2 km/s. The upward-flowing peak is at a vertical velocity of 8.5 km/s, while the downward-flowing peak is at a vertical velocity of -7.4 km/s. A significant portion of the distribution is spread out between the two peaks; $f(v_x, v_z)$ is 38% of its maximum value at the saddle point, $(v_x, v_z) = (15.2, -2.6)$ km/s. The vertical asymmetry in the distribution is slight, and may reflect a slight misalignment of the vertical beam with the z-axis.

The $x = 50$ cm reconstruction in Figure 14(b) shows counterflowing plasmas with a mean axial velocity of 18.2 km/s. The upward-flowing peak is at a vertical velocity of 1.8 km/s, while the downward-flowing peak is at a vertical velocity of -2.0 km/s. A significant portion of the distribution remains spread out between the two peaks, with $f(v_x, v_z) = 43\%$ of the maximum at the saddle point, $(v_x, v_z) = (18.2, -0.9)$ km/s. As before, the upwards population is slightly larger, which tends to confirm a slight misalignment of the vertical beam with the z-axis.

Figures 15(a) and 15(b) show the axial variation of ion axial velocity along the thruster axis. Here, the velocity increase monotonically with distance.

Figures 16(a) and 16(b) show the variation of ion axial temperature along the P5 discharge channel axis.

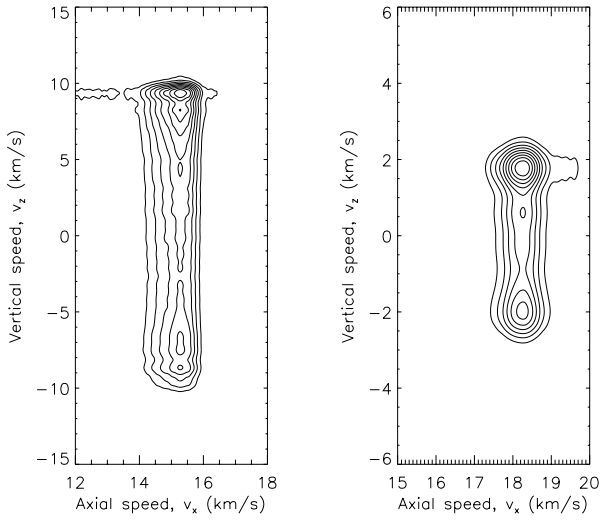

(a) 10 cm, 3.0 kW. (b) 50 cm, 3.0 kW.

Figure 14: Two-dimensional velocity distribution $f(v_x, v_z)$ downstream of P5 centerline, normalized so $f \leq 1.0$. Contour lines are at $f = [0.1, 0.2, \ldots 0.9]$.

5 Discussion

Previous multiplex LIF measurements by Williams[6] of the P5 plume indicated axial ion velocities at $x = 10$ cm on the discharge chamber centerline of 16.0 km/s at 1.6 kW and 17.0 km/s at 3.0 kW. A check run at 3.0 kW during recent (unpublished) multiplex LIF measurements of the P5 plume returned an axial ion velocity at the same location of 20.12 km/s. These values neatly straddle the speed measured by axial-injection LIF, while the $\pm 16\%$ error band implied by the multiplex values is within the 20% uncertainty caused by a stackup of 2% uncertainties in angle and bulk velocity.

Haas[13] reported a P5 specific impulse of 1580 s at 1.6 kW and 1670 s at 3.0 kW. Adjusted for the ratio of anode flow rate to total flow rate, this corresponds to expected axial velocities of 17.0 km/s at 1.6 kW and 17.2 kW at 3.0 kW. These values are 9.2% and 7.9% lower than the maximum axial velocities measured by direct-injection LIF, but match the axial velocity in the region 1 to 2 cm cm downstream of the thruster exit plane.

Williams[6] noted a 90 V increase in axial ion energy downstream of the P5 discharge. The "near-field" range

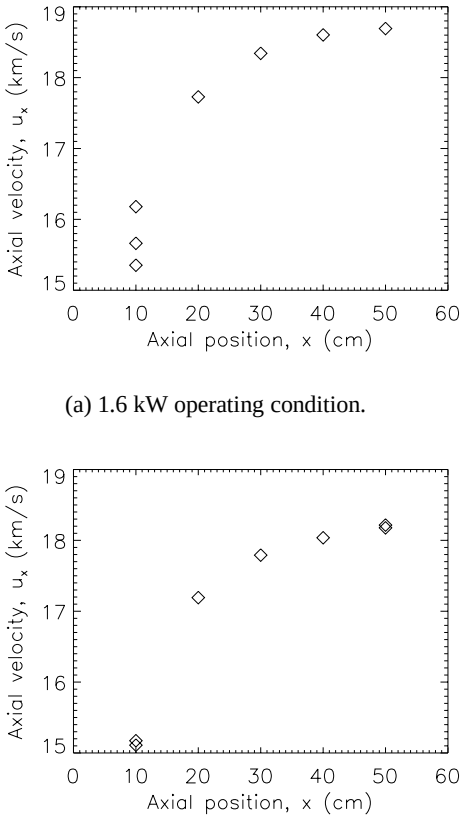

(a) 1.6 kW operating condition.

(b) 3.0 kW operating condition.

Figure 15: Axial ion velocity vs. axial position along P5 centerline (y = 0 cm).

covered in that study, however, stopped 10 cm downstream of the exit plane, missing the point of maximum velocity and the subsequent deceleration. Subsequent plasma potential measurements by Haas[15] showed an 85 V drop in plasma potential from $x = 0$ to $x = 10$ cm at 1.6 kW, which is 16% less than the 101 V increase in ion axial energy we measured over the same range. Though the inherently intrusive nature of probe-based diagnostics might account for the 16 V difference in results, a more sophisticated hypothesis is that ions arriving at an interrogation point on the discharge channel centerline do not originate on that same centerline. Future lateral-injection LIF of the P5 plume will test this hypothesis.

Cedolin[4] also noted increasing axial velocity downstream of the Stanford 260 mW Hall thruster discharge, as well as a "levelling off" around 3.0 cm downstream;

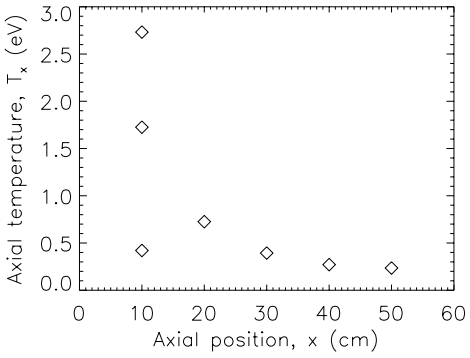

(a) 1.6 kW operating condition.

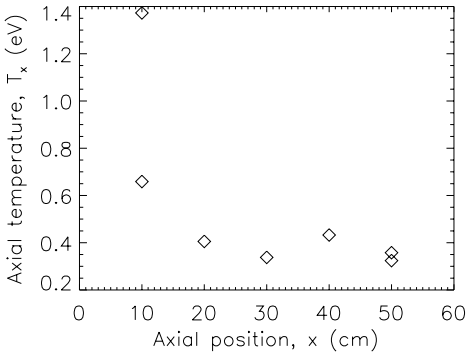

(b) 3.0 kW operating condition.

Figure 16: Axial ion temperature vs. axial position along P5 centerline (y = 0 cm).

unfortunately, this study also failed to note any deceleration in the remaining 1.0 cm of the survey. The loss of axial velocity downstream of $x = 20$ cm is probably not caused by ion-neutral collisions; the mean free path (MFP) for Xe II - Xe I elastic collisions at these conditions is almost 30 m, while the Xe II - Xe I charge exchange (CEX) MFP is 11 m. Ion-ion elastic collisions, with a MFP of 60 cm, are a more likely cause of the perceived velocity loss. The sudden departure of the axial temperature profile from the predicted kinematic compression trend at $x = 20$ cm lends credence to the collisional hypothesis. Future lateral sweeps at this location, and possibly testing at lower base pressures, will shed more light on this effect.

The centerline velocity distribution peaks shown in Fig. 14(a) and 14(b) are consistent with collisionless expansion from an annular discharge. Electric field effects downstream of the exit plane are not negligible; not only do the bulk velocity vectors fail to line up on position vectors from the discharge, but the velocity magnitude of the peaks rises from 17.1 km/s at 10 cm to 18.3 km/s at 50 cm. The portion of the distribution between peaks, which we will call the "mixing population," is especially interesting, as ions with very low vertical velocity magnitudes cannot follow a straight line from the discharge to the centerline. Though the centerline distributions are likely to be two-stream unstable, it is unclear if this instability is responsible for the mixing population. Future lateral LIF sweeps, combined with ion trajectory simulations, will help explain this portion of the distribution.

By converting velocity distributions deconvolved from LIF spectra to energy space, we can compare our data to existing mass spectrometer data. Figure 17(a) shows a Molecular Beam Mass Spectrometer (MBMS) energy spectrum taken by Gulczinski[16] 10 cm downstream of the discharge channel centerline at 1.6 kW. The MBMS primary peak occurs at an ion energy per unit charge of 260 V, while a second, broader peak occurring at 350 V (approximately 4/3 of the primary peak energy) is a Xe IV population caused by a Xe V - Xe I CEX collision. Figure 17(b) shows an ion energy distribution $g(E_x)$, transformed from the deconvolved velocity distribution at the same location by the relation

$$g(E_x) = \sqrt{\frac{2E_x}{m^3}} f(v). \tag{36}$$

The LIF primary peak occurs at 235 V, with a second, broader peak centered at 270 V. The primary peak widths are quite similar, as should be expected when the axes are properly transformed between velocity and energy space. Both distributions also have a pronounced low-energy tail. The 25 V difference between the primary peak energies may be explained by the 15 V plasma potential measured by Haas[15]; ions falling from this potential into a parallel-plate energy analyzer with grounded entry and exit slits will indicate a higher energy than LIF. Since our LIF scheme can only detect Xe II, the LIF secondary peak is not a direct CEX population, as the only Xe II peaks from CEX distributions occur at integral multiples of the primary peak energy[17]. Since the ion-ion MFP at these conditions is 60 cm, Xe III - Xe II elastic collisions are the most likely explanation for the LIF secondary peak.

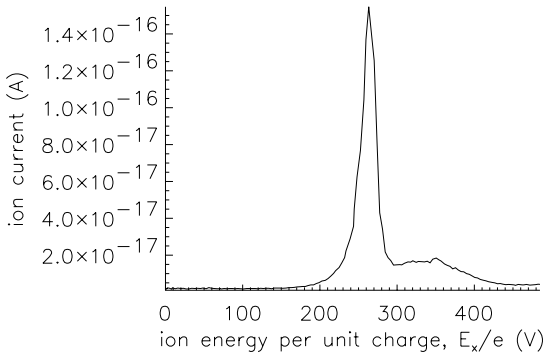

(a) Ion energy distribution from MBMS data.

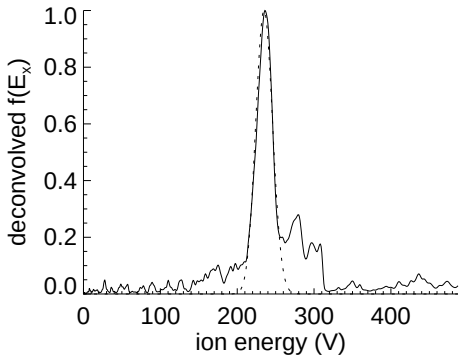

(b) Ion energy distribution from LIF data.

Figure 17: Energy distributions at 1.6 kW, (x, y) = (10., 7.37) cm.

6 Conclusions

The deconvolution of axial-injection LIF spectra has been demonstrated as a viable diagnostic technique for Hall thruster plumes. Axial velocities were measured with less than 2% precision error, while axial temperatures were determined within a 40% error band. Previous multiplex LIF measurements of axial velocity bracketed the values measured by axial-injection LIF, showing both the accuracy of axial-injection LIF and the large error bands inherent in multiplex LIF.

Energy distributions transformed from LIF deconvolutions compared well with MBMS energy distributions at the same location. The primary peaks were shown to have nearly identical widths, while the peak location shift was commensurate with the floating potential at the measurement location.

An acceleration region was shown to extend 20 cm downstream of the P5 exit plane, followed by a deceleration region. Axial temperatures during 1.6 kW operation tended to decrease with increasing axial velocity and increase with decreasing axial velocity, supporting the hypothesis of kinematic compression. No such effect was observed during 3.0 kW operation, where a collisionless model may be less reasonable.

Future investigations of lateral velocity distributions will provide a more complete depiction of the P5 plume. The assumption of statistical independance is untested, and may well be unfounded in Hall thruster plumes; tomographic reconstruction of a full, 180° sweep will allow verification of this assumption. The role of facility pressure on the deceleration zone is also unknown, while extending axial-injection LIF techniques into the discharge channel is a logical progression of the present work. Axial-injection LIF also shows promise for ion engine experiments, as we expect to show in future near-field plume and discharge chamber characterization of an NSTAR-derivative ion engine.

7 Acknowledgements

This research was supported by the Air Force Office of Scientific Research grants F49620-00-1-0201 and F49620-01-1-0061 (Dr. Mitat Birkan is the contract monitor for both). D.A.H. acknowledges support from the NASA Glenn Research Center via Grant NAG3-2216, monitored by J. Sovey and M. Domonkos. The authors are greatly appreciative of this support.

We would also like to thank the graduate and undergraduate students at PEPL for their assistance in experimental setup and operation, and the Department's technical support staff for their aid with facility repairs and modifications.

References

[1] D. Keefer et al. "Multiplexed laser induced fluorescence and non-equilibrium processes in arcjets." In *Proceedings of the 25the Plasmadynamics and Lasers Conference*. AIAA-94-2656, July 1992.

[2] J.A. Pobst and I.J. Wysong. "Laser induced fluorescence of ground state hydrogen atoms at nozzle exit of an arcjet plume." In *Proceedings of the 26th AIAA Plasmadynamics and Lasers Conference*. AIAA-95-1973, June 1995.

[3] D. H. Manzella. "Stationary plasma thruster ion velocity distribution." In *Proceedings of the 30th Joint Propulsion Conference*. AIAA-94-3141, June 1994.

[4] R. Cedolin et al. "Laser-induced fluorescence study of a xenon hall thruster." In *Proceedings of the 33rd Joint Propulsion Conference*. AIAA-97-3053, July 1997.

[5] G.J. Williams Jr. et al. "Laser induced fluorescence measurement of ion emitted from hollow cathode." In *Proceedings of the 35th Joint Propulsion Conference*. AIAA-99-2862, June 1999.

[6] G.J. Williams Jr. et al. "Laser induced fluorescence measurement of ion velocities in the plume of a hall effect thruster." In *Proceedings of the 35th Joint Propulsion Conference*. AIAA-99-2424, June 1999.

[7] H. Kopfermann. *Nuclear Moments*. Academic Press, 1958.

[8] C.C. Candler. *Atomic Spectra and the Vector Model*. Van Nostrand, 1964.

[9] C.R. Bingham et al. "Collinear fast-beam laser spectroscopy experiment: measurement of hyperfine structure and isotope shifts in Xe II." *Nuclear Instruments and Methods*, 202(147), May 1982.

[10] P. A. Jansson. *Deconvolution of images and spectra*. Academic Press, 1997.

[11] J.T. Verdeyen. *Laser Electronics*. 3rd ed., Prentice-Hall, 1995.

[12] S. L. Kaufman. "High-resolution laser spectroscopy in fast beams." *Optics Communications*,17(309), June 1976.

[13] J.M. Haas et al. "Performance characteristics of a 5 kw laboratory Hall thruster." In *Proceedings of the 34th Joint Propulsion Conference*. AIAA 98-3503, July 1998.

[14] H.W. Coleman and W.G. Steele Jr. *Experimentation and uncertainty analysis for engineers*. John Wiley & Sons, 1989.

[15] J.M. Haas. *Low-perturbation interrogation of the internal and near-field plasma structure of a Hall thruster using a high-speed probe positioning system.* Ph.D. dissertation, Dept. of Aerospace Engineering, University of Michigan, Jan 2001.

[16] F. S. Gulczinski et al. "Near-field ion energy and species measurements of a 5 kW laboratory Hall thruster." In *Proceedings of the 35th Joint Propulsion Conference*. AIAA 99-2430, June 1999.

[17] F. S. Gulczinski. *Examination of the structure and evolution of ion energy properties of a 5 kw class laboratory Hall effect thruster at various operational conditions.* Ph.D. dissertation, Dept. of Aerospace Engineering, University of Michigan, Aug 1999.